



**Dislocation driven spiral and non-spiral growth in layered chalcogenides: morphology, mechanism, and mitigation**

Journal:	<i>Nanoscale</i>
Manuscript ID	NR-ART-03-2018-002280.R1
Article Type:	Paper
Date Submitted by the Author:	02-Jun-2018
Complete List of Authors:	Nie, Yifan; The University of Texas at Dallas, Barton, Adam; The University of Texas at Dallas Addou, Rafik; University of Texas at Dallas, Zheng, Yongping; University of Texas at Dallas, Walsh, Lee; The University of Texas at Dallas Eichfield, Sarah; Penn State University, Yue, Ruoyu; The University of Texas at Dallas Cormier, Christopher; The University of Texas at Dallas Zhang, Chengxi; University of Texas at Dallas, Materials Science and Engineering Wang, Qingxiao; University of Texas at Dallas, Materials Science and Engineering Liang, Chaoping; University of Texas at Dallas, Materials Science and Engineering Robinson, J; The Pennsylvania State University, Kim, Moon; the University of Texas at Dallas, Materials Science and Engineering Vandenberghe, William; The University of Texas at Dallas Colombo, Luigi; Texas Instruments Inc, Cha, Pilyoung; Kookmin University, School of Advanced Materials Wallace, Robert; University of North Texas at Dallas, Hinkle, Christopher L.; University of Texas at Dallas, Materials Science and Engineering Cho, Kyeongjae; The University of Texas at Dallas,



Cite this: DOI: 10.1039/xxxxxxxxxx

## Dislocation driven spiral and non-spiral growth in layered chalcogenides: morphology, mechanism, and mitigation<sup>†</sup>

Yifan Nie,<sup>a</sup> Adam T. Barton,<sup>a</sup> Rafik Addou,<sup>a</sup> Yongping Zheng,<sup>a</sup> Lee A. Walsh,<sup>a</sup> Sarah M. Eichfeld,<sup>b,c</sup> Ruoyu Yue,<sup>a</sup> Christopher Cormier,<sup>a</sup> Chenxi Zhang,<sup>a</sup> Qingxiao Wang,<sup>a</sup> Chaoping Liang,<sup>a</sup> Joshua A. Robinson,<sup>b,c</sup> Moon Kim,<sup>a</sup> William Vandenberghe,<sup>a</sup> Luigi Colombo,<sup>d</sup> Pil-Ryung Cha,<sup>e</sup> Robert M. Wallace,<sup>a</sup> Christopher L. Hinkle,<sup>a</sup> and Kyeongjae Cho<sup>\*a</sup>

Received Date

Accepted Date

DOI: 10.1039/xxxxxxxxxx

www.rsc.org/journalname

Two-dimensional materials have shown great promise for implementation in next-generation devices, however, controlling the film thickness during epitaxial growth remains elusive and must be fully understood before wide scale industrial application. Currently, uncontrolled multilayer growth is frequently observed, and not only does this growth mode contradict theoretical expectations, but it also breaks the inversion symmetry of the bulk crystal. In this work, a multiscale theoretical investigation aided by experimental evidence is carried out to identify the mechanism of such an unconventional, yet widely observed multilayer growth in the epitaxy of layered materials. This work reveals the subtle mechanistic similarities between multilayer concentric growth and spiral growth. Using the combination of experimental demonstration and simulations, this work presents an extended analysis on the driving forces behind this non-ideal growth mode, and the conditions that promote the formation of these defects. Our study shows that multilayer growth can be a result of both chalcogen deficiency and excess: the former causes metal clustering as nucleation defects, and the latter generates in-domain step edges facilitating multilayer growth. Based on this fundamental understanding, our findings provide guidelines for the narrow window of growth conditions which enables large-area, layer-by-layer growth.

## 1 Introduction

The controlled epitaxy of two-dimensional (2D) materials, such as layered chalcogenides, is a necessary requirement for their in-

dustrial application in novel nanoelectronic and optoelectronic devices<sup>1–8</sup>. Following the successful growth of high quality graphene via the chemical vapor deposition (CVD) method<sup>9,10</sup>, similar efforts have been made to develop epitaxial methods for high quality growth other 2D materials<sup>11–20</sup>, most of which are compound materials. Despite these significant technical advances, a universal growth method that can precisely control the film uniformity, layer number, and defect level is still yet to be established. To address the challenge, an industry-acceptable growth method should also be compatible with the device-processing environment, where contamination such as inorganic salts, for example, cannot be used. For this reason, this research utilizes experimental results from films grown by molecular beam epitaxy (MBE) in concert with theoretical simulations to probe the mechanistic aspects of nucleation and growth behavior in a number of 2D systems.

Recent experimental research has shown that films synthesized by bottom-up methods exhibit polycrystalline characteristics. The issues associated with the controlled crystal growth in 2D materi-

<sup>a</sup> Department of Materials Science and Engineering, The University of Texas at Dallas, Richardson, Texas 75080, United States

<sup>b</sup> Department of Materials Science and Engineering, The Pennsylvania State University, University Park, Pennsylvania 16802, United States

<sup>c</sup> Center for Two-Dimensional and Layered Materials, The Pennsylvania State University, University Park, Pennsylvania 16802, United States

<sup>d</sup> Texas Instruments Incorporated, 13121 TI Boulevard, Dallas, Texas 75243, United States

<sup>e</sup> School of Advanced Materials, Kookmin University, Jeongneung-gil 77, Seongbuk-gu, Seoul, 136-702, Korea

\* E-mail: kjcho@utdallas.edu; Tel: +1 (972)883 2845

<sup>†</sup> Electronic Supplementary Information (ESI) available: Additional PFM simulation on the effect of flux and reaction anisotropy, additional DFT calculation on the growth rate comparison of different edges, and detailed characterization of the MBE Bi<sub>2</sub>Se<sub>3</sub>. See DOI: 10.1039/b000000x/

als can be broken down into intergranular and intragranular categories. The intergranular category includes grain size<sup>21–23</sup>, grain boundaries<sup>24–26</sup>, and grain registry<sup>27</sup>. The intragranular aspects include the domain morphology<sup>28–30</sup>, imperfections<sup>31–33</sup>, and control of the number of layers per grain<sup>23,34–36</sup>. Although many of these issues have been improved through experimental and theoretical investigations, the fundamental understanding of the thickness (layer number) control in each grain is still in its infancy and requires much more attention before these materials can be used in industrial applications.

Since the early demonstrations of van der Waals epitaxy, it has been argued that, due to the absence of strong bonding in the vertical growth direction, lattice mismatch does not cause an accumulation of strain, which can cause island growth mode with strain relaxation (e.g., Ge islands on Si)<sup>37,38</sup>. As a result, theory suggests that under ideal conditions, the growth of the layered materials should follow the layer-by-layer growth mode. Moreover, both the thermodynamic and kinetic analyses show that, when stabilized by the substrate, transition metal dichalcogenides (TMDs), for example, should not deviate from the layer-by-layer growth mode<sup>35,36</sup>. The resulting domains of layer-by-layer grown 2H-TMDs are expected to show alternately-oriented stacked triangles according to layer structures of 2H bulk phase. This growth pattern would give the stable stacking sequence and minimizes the edge energy. With the nucleation of each layer an independent events from the underlying layers, the center of the nucleus on each layer should rarely overlap<sup>39</sup>. However, during the epitaxy of the 2H-TMDs, the observation of concentric triangles with the same stacking orientation occurs more often than expected<sup>40–43</sup>, which indicates a different nucleation and growth mechanism. In addition to the 2H-TMDs, multilayer growth with broken inversion symmetry can also be observed in the epitaxy of in hexagonal boron nitride<sup>44</sup>. The continuous formation of this metastable structure strongly indicates that the nucleation and growth of each layer is dependent on the underlying layer. Yue *et al.* demonstrated that the concentric triangles and the correlated multilayer growth can be obtained under chalcogen deficient conditions, due to the clustering of metal atoms (Figure 1a)<sup>23</sup>. However, even under growth conditions with a sufficient chalcogen flux, correlated multilayer growth is still observed, counter to theoretical predictions (circled region in Figure 1b). In the parlance of crystal growth, the concentric multilayer growth is also referred to as the close-looped growth, in contrast to open-loop, spiral growth from surface defects (Figure 1c-f).

In addition to the multilayer growth with closed loops, another type of multilayer growth with more recognizable strong inter-layer interaction is the multilayer growth driven by screw dislocations<sup>45–56</sup>. Various combinations of screw dislocations have been suggested as causing various patterns of spiral growth observed in experimental epitaxy (Figure 1b-f)<sup>45</sup>. This growth mode shares many similarities with the close-looped multilayer growth, with concentric triangular layers that do not adhere to the bulk crystal inversion symmetry. Such similarities may not just be coincidence. It has been demonstrated that a spiral growth mode can result in a close-looped termination, obscuring the spiral origin<sup>57</sup>. Therefore, it is important to rigorously examine spiral growth

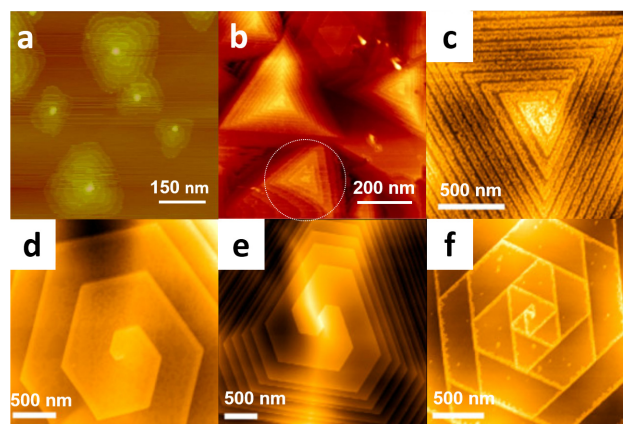


**Fig. 1** Experimentally observed multilayer growth with different morphologies. (a): Atomic force microscopy (AFM) image of molecular beam epitaxy (MBE) grown  $\text{WSe}_2$ . (b): Scanning tunneling microscopy (STM) image ( $V_b=1.8$  V,  $I_t=0.5$  nA) of  $\text{WSe}_2$  grown by the metal-organic CVD (MOCVD). A concentric triangle domain without spiral line is circled. (c-f): AFM images of CVD grown  $\text{WSe}_2$ , reproduced from the reference<sup>45</sup> with the permission of ACS.

modes and determine whether there is a connection between spiral growth and the concentric multilayer growth observed in experiment.

In this work, the cause of the multilayer growth in the layered chalcogenides (primarily TMDs and  $\text{Bi}_2\text{Se}_3$ ) is investigated. Aided by a phase field model<sup>58–60</sup>, we are able to demonstrate the mechanistic similarity between concentric multilayer growth and spiral growth, revealing the correlated nature in the initiation and growth of each layer. We explain the experimentally observed spiral morphologies by connecting their origin with the topographical and atomic features of underlying defects from both the substrate as well as in-grain defects. In addition to the reported growth morphologies and structures, our model calculates a new growth mode driven by the coupling of screw dislocations, which we then experimentally demonstrate for the first time through the MBE growth of  $\text{Bi}_2\text{Se}_3$ . This new mechanism explains the frequently observed multilayer growth that breaks the inversion symmetry expected for 2H crystals, which superficially resembles spiral growth, but exhibits no spiral lines. The mechanism is transferrable to different material systems, especially chalcogenides, with elements of high dimerization capability. We then extend the discussion, through first-principles investigations, to the experimental conditions that facilitate this mechanism. With the conditions articulated, we can provide the experimental window that will enable thickness controlled, layer-by-layer epitaxy of 2D materials.

## 2 Phase field model

The Phase field model is based on an approach that uses a continuous order parameter (denoted by  $\psi$ ) to distinguish different phases. The Landau theory of phase transformation treats  $\psi$  as a state variable, and therefore its spatial distribution  $\psi(\vec{x})$  can be used to determine the free energy of the system<sup>58</sup>. In the following discussions, we consider a two-dimensional isothermal system, so the temperature dependency is dropped from the rest

of the discussion.

The base equations of a phase-field model for the layered growth of a solid include the kinetics of two fields: 1) the distribution of the order parameter ( $\psi$ ), which describes the phase transformation, and 2) the concentration field of the precursor ( $u$ ), which is governed by the conservation of mass<sup>59</sup>:

$$\tau_\psi \frac{\partial H}{\partial t} = -\frac{\partial H}{\partial \psi} = W^2 \nabla^2 \psi + \sin[\pi(\psi - \psi_s)] + \lambda u \{1 + \cos[\pi(\psi - \psi_s)]\}, \quad (1)$$

$$\frac{\partial u}{\partial t} = D \nabla^2 u - \frac{u}{\tau_s} + F - \frac{1}{2} \frac{\partial \psi}{\partial t}. \quad (2)$$

In Equation (1),  $\psi/2$  represents the height of the epilayer surface, and  $\psi_s/2$  is the height of the surface of the substrate (or the underlying layer), in units of monolayer thickness. The derivative of the bulk free energy density takes the form of a sinusoidal function of  $\psi$  with equally spaced multiple minima at  $\psi - \psi_s = 2n + 1$ , in which  $n$  is an integer, and can be interpreted as the deposited layer number with respect to the reference of  $\psi_s$ .  $W$  represents the interface width. The last term in Equation 1 connects the two kinetic equations with the coupling constant  $\lambda$ .  $D$  is the diffusivity of the precursor,  $F$  is the flux of the precursor, and  $\tau_\psi$  and  $\tau_s$  are the characteristic times of adatom attachment and evaporation, respectively. To simulate a screw dislocation at the origin,  $\psi_s$  takes the value that makes  $\pi\psi_s = \text{atan2}(y, x)$ , in which  $\text{atan2}(y, x)$  is the polar angle in the x-y plane, and is defined as:

$$\text{atan2}(y, x) = \begin{cases} 2 \arctan\left(\frac{y}{\sqrt{x^2 + y^2 + x}}\right), & \text{if } x > 0 \text{ or } y \neq 0, \\ \pi, & \text{if } x \leq 0 \text{ and } y = 0. \end{cases} \quad (3)$$

To simulate multiple screw dislocations, the  $\psi_s$  takes the value of

$$\psi_s = \sum_i s_i h_i \left[ \left( \frac{\text{atan2}(y - y_i, x - x_i) + \varphi_i}{\pi} + 1 \right) \bmod 2 - 1 \right], \quad (4)$$

where for each screw dislocation,  $s_i$  is the chirality (or the sign) of the helix, with the value of  $\pm 1$ ;  $h_i$  is the height of the ridge, defining the elevation after a full rotation, in units of monolayer thickness;  $(x_i, y_i)$  is the coordinate of the core, and  $\varphi_i$  is the polar angle of the ridge. The modulo operation wraps any angle  $\text{atan2}(y - y_i, x - x_i) + \varphi_i$  down to its coterminal angle within  $[-\pi, \pi]$ . Visualizing the above representations, a single screw dislocation has a contour of Figure 2a, and a pair of screw dislocations with the same sign are like Figure 3a.

As the monolayers of many of the most widely studied 2D materials (except for graphene) possess structural trigonal symmetry, we include this trigonal symmetry in the simulation and investigate its effect on the growth dynamics. The edge coefficient  $W$  in Equation (1) can be a function of the interfacial orientation, measured by the direction of  $\psi$  represented in polar angle  $\theta$ <sup>60,61</sup>:

$$W(\theta) = W_0 \{1 + \delta [1 + \cos(v\theta)]\}, \quad \theta = \text{atan2}\left(\frac{\partial \psi}{\partial y}, \frac{\partial \psi}{\partial x}\right), \quad (5)$$

in which  $\delta$  is the anisotropy strength, and  $v$  is an integer that defines the rotational symmetry of the island. For trigonal symmetry,  $v$  takes the value of 3. It is noteworthy that once  $W$  becomes a

**Table 1** Parameters used in the phase-field simulations.

Parameters	Symbol	Value
Characteristic time of adatom attachment	$\tau_\psi$	1
Characteristic time of adatom desorption	$\tau_s$	$10^7$
Coupling constant	$\lambda$	19.591
Diffusion coefficient	$D$	10
Interfacial energy coefficient	$W_0$	1
Anisotropy strength	$\delta$	0.05

functional of  $\psi$ , the variation differentiation of  $H[\psi]$  in Equation (1) should be performed properly<sup>62</sup>.

In addition to the structural anisotropy, in principle,  $D$  can be a function of the polar angle to simulate the diffusion anisotropy of the substrate. In this work, the substrate is assumed to be isotropic by setting  $D$  uniformly across the substrate. The values of the parameters employed in the simulation are listed in Table 1. The selection of the parameters follows the reference<sup>59</sup>. Without loss of generality, the time scale and the length scale are non-dimensionalized with respect to  $\tau_\psi$  and  $W_0$ , respectively. The model can always rescale space and time so that only  $D$  and  $\lambda$  are the independent variables<sup>60</sup>. For additional details and justification of the model, please refer to the Supporting Information.

## 3 Results and discussions

### 3.1 Spiral multilayer growth

The common method for categorizing the 2D materials growth morphology is based on the shape of the flakes, sorting them into the triangular (Figure 1b,c), hexagonal (Figure 1d,f), and mixed types (Figure 1e). Although it is straightforward, this method does not explicitly reflect the growth mechanism or the material properties, such as the stacking sequence. In this work, we use a different approach, starting from the defects and investigating the causal relationship between those defects and the resultant flake morphology. In this way, we are able to propose the possible cause of the various spiral and concentric triangle growth behaviors observed in the experiments. Taking the values of parameters that relate the phase-field model to the sharp-interface conditions in the Burton-Cabrera-Frank (BCF) theory<sup>60,63,64</sup> (Table 1), we investigate the numerical solutions that have not been explicitly solved previously.

The most extensively studied case of spiral growth in layered materials is of the TMD family. Among their spiral growth observed in the experiments, the majority takes the form of a trigonal growth with only one spiral line (see Figure 1b). This can be easily identified as the continuous growth of a monolayer TMD along one ridge of the screw dislocation (Figure 2a). This basic yet prevalent case will be the building block to explain the more complicated spiral growths. Karma and Plapp have analyzed that, in steady state, the spiral rotation frequency is proportional to the flux ( $F$ )<sup>60</sup>. The model in this work has confirmed this relation (See the Supporting Information for details), which indicates that during a spiral growth, the vertical versus lateral growth can be controlled by the flux. Assuming the same base area, the flake

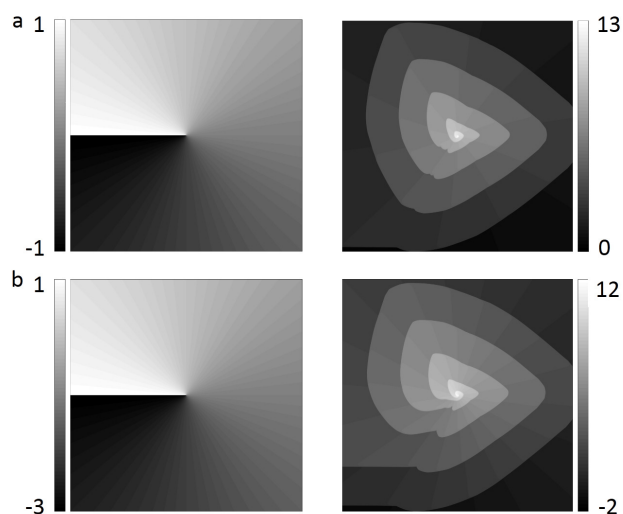


**Fig. 2** Phase-field simulation result: the contour of  $\psi_s$  (left panels) and  $\psi$  (right panels) of the spiral growth driven by single screw dislocations with different height. (a) The step height equals the thickness of a monolayer, and the growth results in a single spiral pyramid. (b) The step height equals twice the thickness of a monolayer, and the resulting domain consists of two parallel spiral lines.

grown under higher flux will have finer spiral threads (Figure S2).

The height of the step edge also has a strong influence on the growth mode. In the case of Figure 2a, the height of the step is equal to the thickness of a monolayer, giving textbook spiral growth; *i.e.*, the surface is elevated one layer after a full rotation, and a new “layer” is generated. When the ridge height equals twice the layer thickness, two layers nucleate and lead to a double spiral growth, which enables each layer to elevate twice its thickness after a full rotation (Figure 2b).

A two-layer-deep screw dislocation is equivalent to the addition of two one-layer-deep screws with the same sign (left- or right-handedness) that overlap with each other. In principle, the ridges of the two dislocations can be apart by an arbitrary angle, and their cores do not necessarily overlap. Figure 3a shows the double-spiral growth driven by two screw dislocations that are  $180^\circ$  apart. While the inner circles preserve the growth pattern of single spirals, the outer rings follow a double-spiral growth that resembles Figure 2b, but is different in the phase, or angle offset ( $\phi_i$  in Equation (4)). When the core distance is shorter than the step width, the inner rings become indistinguishable (Figure 3b).

The comparison of the double-spiral growth driven by different topography of the substrate reveals the correlation between the domain morphology and the properties of the underlying imperfections. First of all, in a given material system, the step width is influenced by the flux. The higher is the flux, the narrower each step is. Secondly, the distance of the dislocation cores can be deduced from the distance between the two spirals, and the angle of the ridges from the phase difference of the spirals.

In addition to the expected trigonal domains most frequently observed (Figure 1b,c), hexagonal domains (Figure 1d,f) and trigonal-hexagonal intermediate cases (Figure 1e) are also observed, albeit at a much lower frequency<sup>45</sup>. These domains can

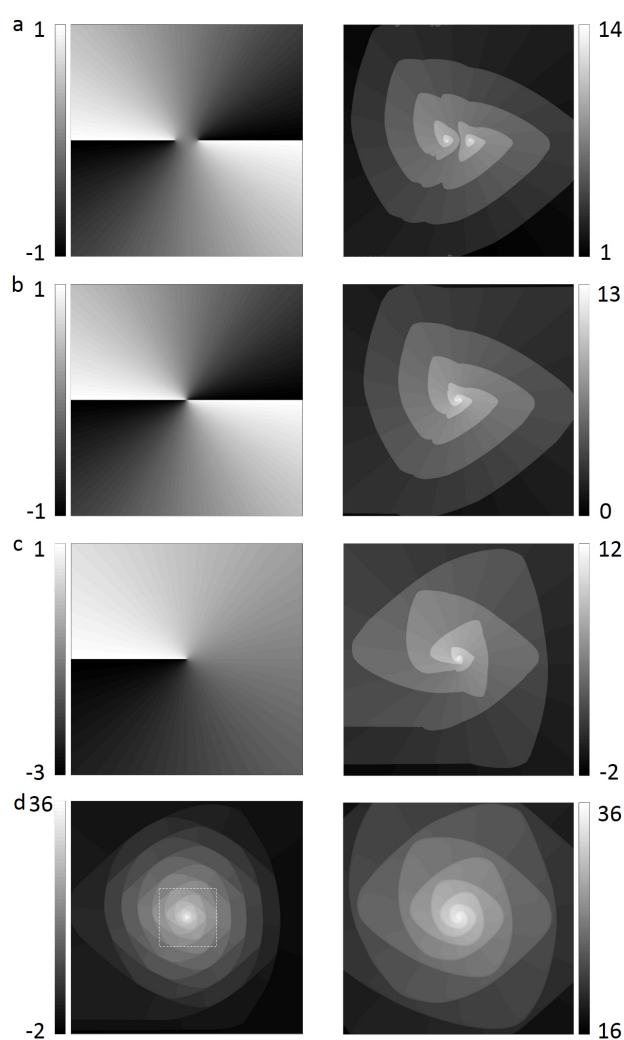


**Fig. 3** (a-c) Phase-field simulation result of double-spiral growths: the contour of  $\psi_s$  (left panels) and  $\psi$  (right panels) of the double spiral growth driven by the combinations of dislocations with the same sign. (d): The growth from the  $\psi_s$  of (c), but at a higher flux. The right panel of (d) shows a zoom-in image of its spiral core. The two separate screw dislocations make it possible for the two spiral growths to assume different orientations, which form the inter-terminating hexagonal shape.

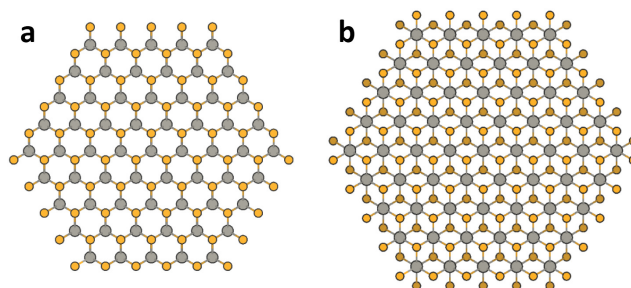


**Fig. 4** Hexagonal flakes of trigonal prismatic (left) and octahedral (right) TMD domains. The gray circles represent metal and the yellow for chalcogen atoms, the bottom layer of which has a darker shade. While the edges for the tri-TMD can be categorized into two groups with fundamentally different structures, the six edges of the oct-TMD domain are structurally equivalent, different only by the interaction with the underlying substrate (not shown).

be further categorized into two sets: those consisting of parallel spiral lines (Figure 1d,e), and those with partially overlapping spirals (Figure 1f). The cause of the parallel spiral lines is as follows. For the epitaxy on an isotropic substrate, the anisotropy of the film is determined by two factors: 1) the inequity of the different edges on the structural stability (tuned by the anisotropy of  $W$  in Equation (1)); and 2) the reactivity differences of the respective edges (tuned by the anisotropy of  $\tau_\psi$ ), both of which depend on the chemical potentials of the precursors. Figure 4 shows the hexagonal domains of TMDs with the trigonal prismatic (tri-TMD, or traditionally but less precisely for a monolayer, 2H) and octahedral (oct-TMD, or 1T) structures, with every edge fully chalcogenized. For the tri-TMD, three of the edges contain the bridge chalcogen atoms only, while the other three edges have dangling chalcogen atoms. Due to the significant difference of the structure and the reactivity of the two types of edges, tri-TMD domains are predominantly trigonal. However, under certain growth conditions, controlled by the ratio of the metal and the chalcogen precursors, the growth rate of the two sets of edges can be comparable, or even equal. When the growth rate of the six edges are equal, the monolayer will grow with the symmetry of a regular hexagon<sup>29</sup>. When the two sets of edges have comparable yet different growth rates, the monolayer will take the intermediate form of a hexagon with trigonal symmetry (Figure 1e). This can be achieved by either of two scenarios: 1) both the reactivity and energy of the two sets of edges are comparable; 2) the energy of the two sets of edges are not equal, but the edges with lower energy are tuned by the precursor environment to have higher reactivity; thus the low energy edges remain due to their thermodynamic stability, and the high energy edges remain due to their kinetic inertia. The stringency of the criteria makes the observation of these growth modes rare (for extended discussion and illustrations, please refer to the Supporting Information). Under these conditions, driven by one or more screw dislocations with the same sign, the domains will be naturally hexagonal. The continuum model can only provide multiple mechanistic possibilities for similar morphologies. Additional atomistic calculations can be used to determine which possibility makes the most physical sense in a specific context, such as the example of MoS<sub>2</sub> in the later sections of this work.

Octahedral TMDs, on the other hand, have both bridge and dangling chalcogen atoms on every edge, therefore the six edges should, in theory, have the same reactivity. However, in reality, the domain is always influenced by the substrate, resulting in the two groups of edges having different reactivity, albeit to a lesser extent than the tri-TMDs (Figure 4b). Therefore, for oct-TMDs, a six-edge flake can be obtained more easily. This has been demonstrated by Wu *et al.* through experiments and phase-field modeling of the spiral growth of SnSe<sub>2</sub><sup>55</sup>.

The other type of hexagonal growth is driven by a distinct mechanism. Instead of parallel spiral lines, they possess two sets of spiral lines that both terminate into each other, forming two alternating sets of trigonal layers with opposite orientation (Figure 1f). Although more complex in appearance, it is the second most frequently observed multi-layer grain type, according to Shearer *et al.*<sup>45</sup> This mechanism is unique for crystals with a three-fold ro-

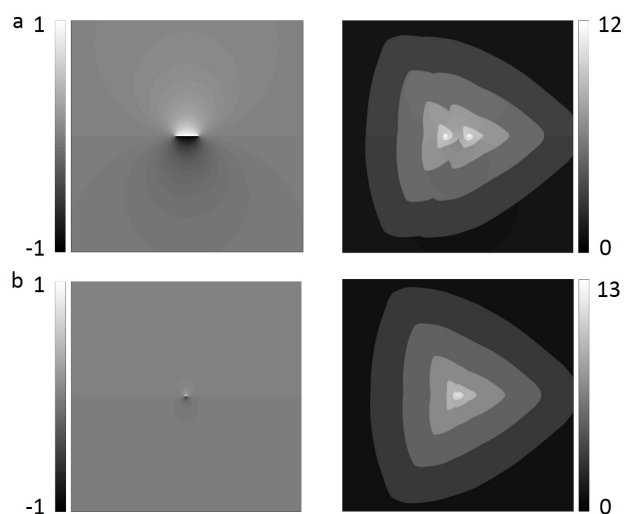


**Fig. 5** Phase-field simulation result of the cancellation of spirals: the contour of  $\psi_s$  (left panels) and  $\psi$  (right panels) of the growth driven by the combinations of dislocations with different signs. Although the inner rings preserve the independent spiral lines, when they meet in the outer rings, the spiral lines cancel out and form closed-loop multilayer growth.

tational symmetry, and a six-fold screw symmetry, represented by the 2H-TMDs such as MoS<sub>2</sub> and WSe<sub>2</sub>. During an epitaxy, these types of materials can form the AB stacking sequence with opposite (180° rotated) orientations. When driven by dislocations that can accommodate two layers, the two spiral growths can assume the opposite orientation, resulting in the spiral growth of alternating triangles (Figure 3c). Under a high flux, when the step width is reduced, the vertices of one trigonal layer will be terminated by the edges of the underlying layer, resulting in hexagonal growth driven by alternating trigonal symmetry (Figure 3d). The stacking sequence of this configuration resembles that of a 2H structure, thus its vibrational spectroscopy resembles the 2H crystal<sup>45</sup>. This type of hexagonal growth is only possible when there are at least two separate spiral growths, as the continuous growth driven by a single screw is in fact a single growth folded into multilayers. This growth mode can only cause translational misalignment, but not the rotational operation essential to establish the AB stacking.

### 3.2 Non-spiral multilayer growth

So far in this work, only the combinations of screw dislocations with the same chirality have been examined, and they can be used to demonstrate the cause of almost all of the complex growth patterns reported in experiments. However, screw dislocations with opposite signs can also couple with each other. When a pair of opposite screw dislocations are in line and share the ridge, they form a short step edge that terminates at the center of the grain (Figure 5a). Driven by this step edge, two opposite spiral growths will be generated, with each growth centered at one of the two ends of the step edge. Interestingly, in the outer rings, the two spirals cancel each other out, and result in closed-loop growth. This type of defect is traditionally named a Frank-Read source<sup>65</sup>. Its spontaneous formation and the growth aftermath have not been

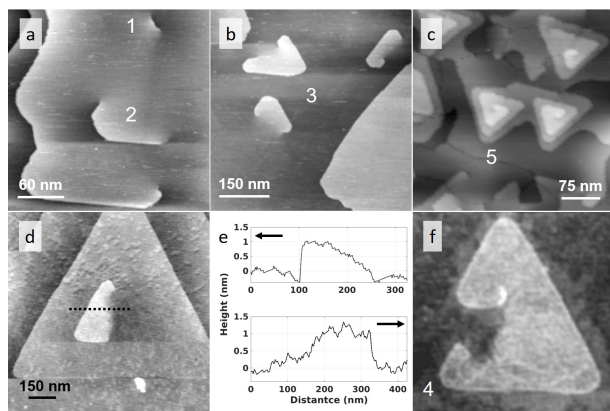


**Fig. 6** STM (a-c) and AFM (d,f) images of the MBE Bi<sub>2</sub>Se<sub>3</sub>. Different stages of the growth driven by a short step edge is labeled in numbers. The height profile along the lines in the AFM images are also included in (e). STM conditions for a, b, and c are  $V_b = 1.7$  V and  $I_t = 0.7$  nA, 2V and 0.5 nA, and 1.7 V and 0.5 nA, respectively.

previously identified and reported in the epitaxy of 2D materials. Bismuth selenide (Bi<sub>2</sub>Se<sub>3</sub>) is a layered chalcogenide known to be prone to spiral growth. Compared to refractory metals such as Mo and W, the clustering of Bi can be better controlled. We have carried out the molecular beam epitaxy (MBE) growth experiment of Bi<sub>2</sub>Se<sub>3</sub> in search of this behavior.

Figure 6 shows the scanning tunneling microscopy (STM) and atomic force microscopy (AFM) images of MBE grown Bi<sub>2</sub>Se<sub>3</sub> (grown on sapphire). Additional characterizations of the Bi<sub>2</sub>Se<sub>3</sub> are shown in more detail in the Supplementary Information. The images show the short step edge assisted growth at different stages. It starts with a short step edge which ends at a pair of opposite screw cores (labeled No. 1 in Figure 6a). Figure 6e is the height profile along the line in Figure 6d. The step-edge drop of  $\sim 1$  nm corresponds to the thickness of a Bi<sub>2</sub>Se<sub>3</sub> monolayer. However, on the other side, the upper layer slopes down continuously into the underlying layer, indicating a climb-up of the step edge, forming a new layer over the other edge now hidden below. Given a long enough growth time, a complete new layer will grow following this mechanism (Figure 6f). If the cores, or the centers of the screw dislocation, have a longer separation distance, the two spirals will grow independently until they are in contact, after which the outer and lower layers will be absent of spiral lines (Figure 6c).

Unlike the grouping of screw dislocations with like sign, screw dislocations with opposite signs are strongly correlated, and attract each other<sup>66</sup>. This makes the coupling of opposite screw dislocations energetically more favorable. When the cores are closer than the step width of the spiral, both the inner circles with separate spirals and the defect itself become less obvious, and the entire domain will assume a closed-loop growth into concentric triangles, with both the size and the layer number increasing (Figure 5b). As previously mentioned, in the epitaxy of materials that should stack in an AB sequence, it is common to observe multilayer growth with concentric triangles, implying a stacking that breaks the inversion symmetry. The cause of the formation of this meta-stable configuration has not been deduced previously. Un-

der chalcogen deficient conditions, concentric multilayer growth of the TMDs can be observed, due to the simultaneous nucleation and growth on the high metal clusters<sup>23</sup> (Figure 1a). However, even under chalcogen-rich conditions that promote spiral growth<sup>49</sup>, concentric triangles can also be observed (circled in Figure 1b), indicating a different mechanism. The above discussions provide one possible cause for this meta-stable configuration. The close-looped growth results in the lateral growth of the outer rings and also the vertical growth of the inner rings, the latter of which is responsible for the generation of new layers. Similar to the case with a single screw dislocation, limited by continuous spiral growth without rotational operations, all layers generated will conform to the original orientation and establish AA stacking. Domains grown following this mechanism share the feature that each new layer is generated in the same spot, therefore all the triangle layers have the same geometrical center.

It is natural that a defective substrate can be the source of dislocations that nucleate and propagate in the epi-film. However, several evidences also indicate such defects can be generated in a flake during its growth, in addition to those from the substrate. First, the spiral growth of the layered chalcogenides can be observed on almost all types of substrates (HOPG, sapphire, SiO<sub>2</sub>, etc.)<sup>40,42,45,49,50,53,55,56</sup>, and the observed spiral density in the resulting flakes is significantly higher than the dislocation density of these substrates. More importantly, it has been reported that the experimental conditions, especially a high chalcogen-metal ratio of the precursors, can influence the generation of the spiral growth for both TMDs and Bi<sub>2</sub>Se<sub>3</sub><sup>45,49,67</sup>. These evidences together strongly indicate that screw dislocations can be generated during the growth of the material, referred to as “growth dislocations”<sup>68</sup>. Next, we will use density functional theory to examine the origins of growth dislocations (and their combinations) in the atomistic scale.

### 3.3 Generation of growth dislocations

The generation of screw dislocations involves a climb-up mechanism. For structures without inversion symmetry within a monolayer, such as 2H-TMDs, the climb-up mechanism starts from the encountering of a pair of edges with different growth rates, as described earlier (Figure 4). Although different in reactivity, the two types of edges are both chalcogen rich. When the two edges are adjacent, they essentially constitute a line of metal vacancies (Figure 7a). Due to the re-configuration of the edges, the linear accumulation of metal vacancies is more stable than the sparse distribution of individual vacancies (Figure 7b-d). The high formation energy of metal vacancies and the requirement of full chalcogenization determine that they can only be formed under chalcogen rich growth conditions. It is also noted that the chalcogenized metal zigzag edge can stabilize itself via chalcogen dimerization. The infinitely long edge (or the part of a long edge away from its end points) can be stabilized more effectively via vertical dimerization, while exerting a strain perpendicular to the vacancy line (Figure 7d). Near the end points of the line vacancy, however, limited by the spatial constraint, the dangling chalcogen atoms can only form planar dimers, which exert contraction along

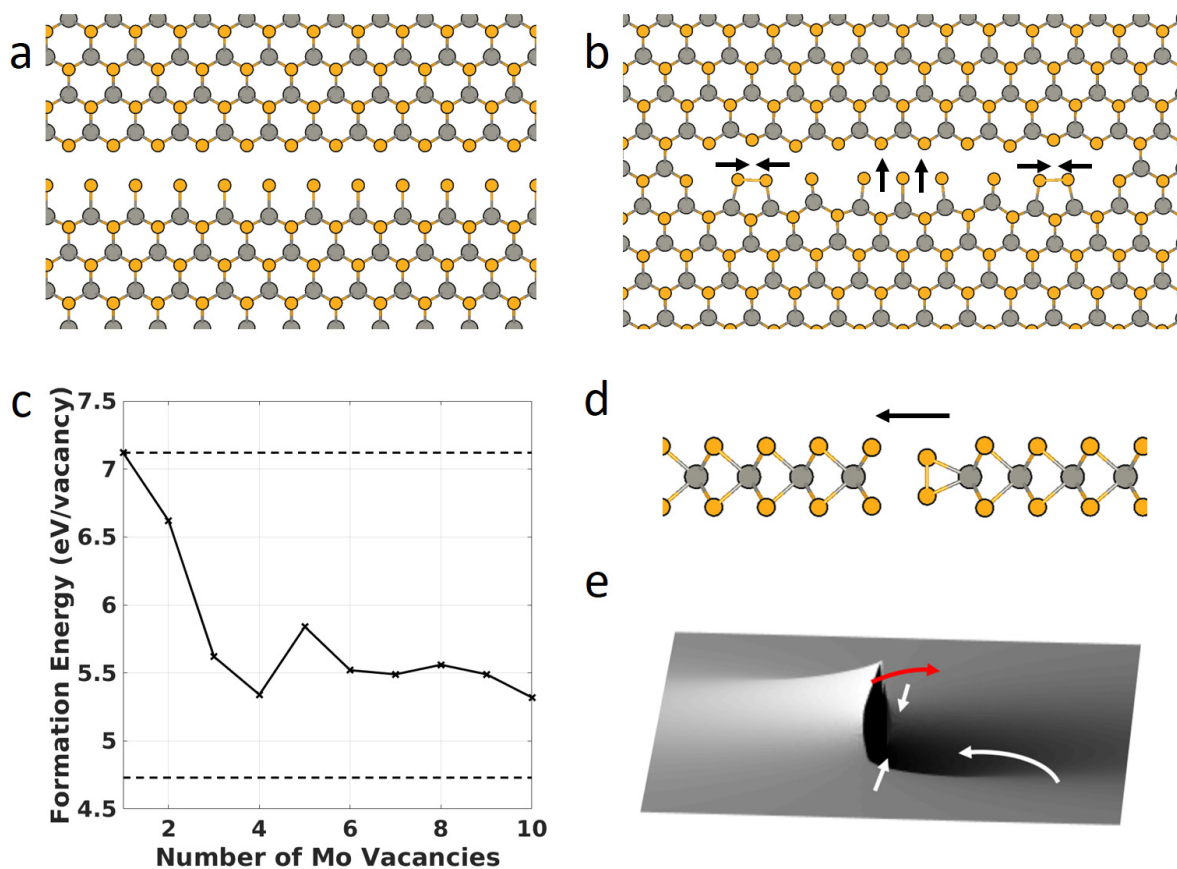


**Fig. 7** (a) The linear alignment of metal vacancies constitutes the encountering of two edges with different growth rate (*cf.* Figure 4a). (b) When the linear arrangement of metal vacancies has finite length, the metal zigzag edge restructure via planar dimerization, with tension along the vacancy line. (c) Change of the formation energy of linearly arranged metal vacancies in monolayer MoS<sub>2</sub> with respect to the linear length. Two reference lines are also plotted: top: the formation energy of sparsely arranged metal vacancies; Bottom: formation energy of infinitely long linearly arranged metal vacancies without terminations. (d) The infinite linear vacancy further stabilizes itself via vertical dimerization, with compression perpendicular to the vacancy line. (e) The in-line and vertical strain together cause corrugation that leads to the defects in Figure 5.

the vacancy line (Figure 7b). This restructuring makes the stable configuration for an adatom (or attached group) on the edge different from its lattice site. An energy barrier exists for its re-configuration from the adsorption site back to the lattice site. Our MoS<sub>2</sub> DFT calculation shows that, due to the differences of the activation energies, the growth rate of the chalcogen zigzag edge is much higher than that of the (chalcogenized) metal zigzag edge (see the Supporting Information for details). The difference in the growth rate of the two adjacent edges, assisted by the crease-inducing strain, promotes the climb-up of the faster edge (Figure 7e). The climb-up mechanism is facilitated by three factors. Firstly, the material must intrinsically consist of edges with different growth rates. Secondly, a chalcogen-rich condition causes the formation of linearly aligned metal vacancies, which forms a pair of adjacent asymmetric edges. Finally, a high growth rate facilitates the fast-growing edge to override the slow and stable edge. Edge lift-up and the subsequent multilayer growth can also be observed in grain boundaries<sup>12,13,39,69</sup>. However, the multilayer growth driven by an in-grain step edge is a unique case as it provides additional assistive strain and guarantees interlayer alignment.

For structures with monolayer inversion symmetry, such as 1T-TMDs and Bi<sub>2</sub>Se<sub>3</sub>, the climb-up mechanism is more straightforward. Similar to 2H-TMDs, the linear alignment of metal vacancies is preferable compared to sparsely distributed vacancies. However, due to the existence of inversion symmetry within the monolayer, the dimerization tendency of dangling chalcogen atoms is resolved between the two adjacent edges (Figure 8). The inter-edge dimerization naturally causes edge lift-up and generate a line of chalcogen dangling bonds. When the line of dangling bonds is ended on both side, it will form the Frank-Read core like for 2H-TMDs. For more detailed analysis, please refer to the Supporting Information.

The linearly aligned metal vacancies can be formed from the evolution of film voids under deposition. As a qualitative demonstration, kinetic Monte Carlo (KMC) simulation<sup>36</sup> of the growth of a TMD from an in-flake void is performed (see Supporting Information for details). The simulation shows that, under deposition conditions, a void will shrink in size. Although the formation of smaller holes are more intuitive, linearly aligned metal vacancies can also be naturally formed. In addition to the two anticipated configurations, another type of defect can be observed from the simulation: two vacancy lines can join and form a 120° angle. This structure also agrees with the proposed lift-up mechanism: in-line contraction at the ends of the line, together with the out-of-line repulsion, under kinetic perturbation, leads to the lift-up of one edge over the other, forming a Frank-Read source.

For the layered materials, the energy expense of a screw dislocation is very different from traditional 3D materials. The energy of a screw dislocation increases linearly with the core length, but only logarithmically with the ridge length, which is often underpinned by the grain size. As a result, for traditional bulk materials, the formation of a screw dislocation is more strongly influenced by its depth than its length. For a layered material, due to the weak interaction between layers, a newly generated screw dislocation does not penetrate to the underlying layers, switching

the role of the screw dislocation from a bulk defect into a surface defect. When the line of metal voids is embedded within a grain, it constitutes a short step edge (Figure 5a, Figure 6a), and results in the multilayer growth of concentric triangles. If the defect line goes through the domain edge, it forms a single screw and causes the multilayer spiral growth. In either way, the layer number increases indefinitely as the lateral grain size increases.

Although spiral growth can produce new crystal structures with various properties, this inability to limit the layer number, and the fact that it always produces a mixture of different spiral structures, indicates that this growth mode must be avoided to produce uniform large-area layered materials with a controlled number of layers. Similar to other defect-driven nucleation-growth mechanisms, the quality of the substrate sets the baseline of the defect level. However, since screw dislocations can also be generated by a fast growth rate in a chalcogen rich environment, to avoid spiral growth, both the growth rate and the chalcogen-to-metal ratio need to be limited during deposition. This is especially important in the early nucleation and growth stages. Once a screw dislocation is formed, it will promote continuous multilayer growth, and cannot be annihilated. However, chalcogen deficiency also results in multilayer growth, due to the clustering of metal atoms, especially refractory metals such as tungsten. A recent study shows that extrinsic particles can also generate Frank-Read source<sup>68</sup>, which explains the similar concentric triangular morphology (Figure 1a). Therefore, there is a “chalcogen-flux window”, instead of a “chalcogen-flux threshold”, that, along with a controlled growth rate and low-defect substrate, enables controlled layer-by-layer growth for the layered chalcogenides. The actual chalcogen-flux window is subject to the specific epitaxy method and experimental conditions such as temperature and the selection of substrate and precursors. The quantitative determination of the chalcogen-flux window for specific cases will be an important continuation of this work. This work, together with our previous investigations, has determined the extrema outside the margin: an insufficient chalcogen flux causes metal clustering, and an excess flux causes spiral growth and/or fractals. Although fractal structures are rich in pairs of adjacent asymmetric edges, the relation between fractal and spiral growth is thus far still unclear, and will be studied in future works. With the mitigation of the defect-driven multilayer growth mechanism, the growth of the 2D compounds returns to a layer-by-layer scheme. Although less favorable, the layer-by-layer growth scheme can also cause multilayer growth.<sup>35,70</sup> Its mechanism of secondary nucleation and homoepitaxy are better understood as van der Waals epitaxy. Our previous studies have demonstrated that the homogeneous nucleation can be mitigated by a higher substrate temperature and a low growth rate<sup>23,36</sup>, which also applies to the secondary homogeneous nucleation.

## 4 Conclusion

In conclusion, this work has explored the various morphologies of spiral structures observed in the epitaxial growth of layered chalcogenides and decomposed them into the combination of screw-dislocation-driven growth mechanisms. In addition to the reported morphologies, the simulation predicts a spiral growth mode with close-looped outer rings, which was experimentally

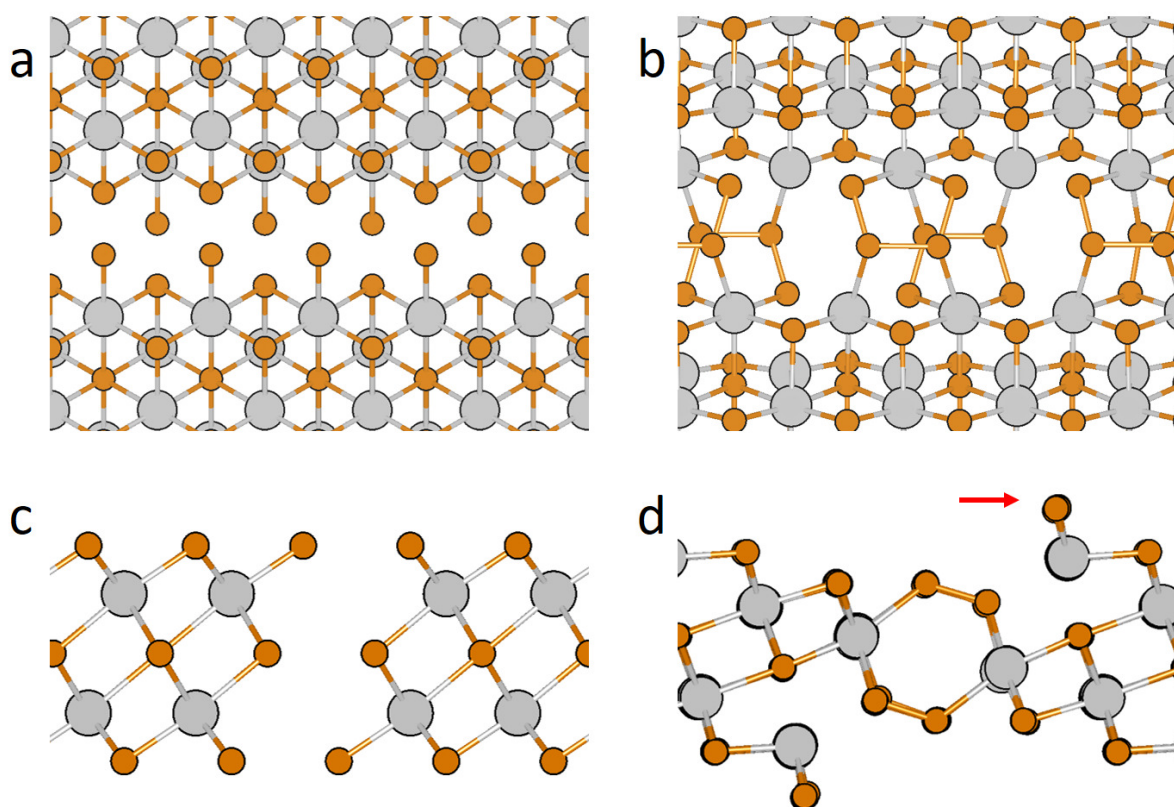


**Fig. 8** The top view (a,b) and side view (c,d) of  $\text{Bi}_2\text{Se}_3$  with linearly arranged metal vacancies, before (a,c) and after (b,d) structural optimization through chalcogen dimerization across the vacancy line. Metal atoms (Bi) are represented by gray orbs, and chalcogen atoms (Se) by yellow orbs. Lift-up of one edge is observed after chalcogen dimerization (d), with a line of dangling bonds exposed (red arrow) as nucleation site.

confirmed for the first time. The proposed mechanism explains the multilayer growth of layered chalcogenides that defies prior theoretical expectation. The formation of the screw dislocation during growth is caused by the dimerization tendency of the chalcogen atoms. This mechanism is transferrable to other materials systems with the similar tendency. Based on these results, we propose that for the layer-number-controlled epitaxy of layered chalcogenides, an upper limit on chalcogen-metal ratio exists, which makes the growth condition window narrower than typically expected.

## 5 Methods

### 5.1 Phase-field method

The code is written in C language. The numerical integration is performed over a  $2,000 \times 2,000$  square grid. Equation (1) is integrated using the forward Euler method, and Equation (2) is integrated with the Crank-Nicolson method, accelerated by the SuiteSparse packages<sup>71</sup>. The zero-flux boundary condition is used.

### 5.2 Density functional theory calculations

The density functional theory simulation is performed with the Vienna Ab-initio Simulation Packages (VASP)<sup>72</sup>. The projector augmented wave potential<sup>73</sup> with Perdew-Burke-Ernzerhof exchange correlation function<sup>74</sup> is used in the calculations. The wavefunction expansion cut-off energy is 400 eV, and the convergence criteria for electronic and ionic relaxation are  $1 \times 10^{-4}$  eV and  $1 \times 10^{-3}$  eV, respectively. The integration over the first Brillouin zone is performed with a  $1 \times 2 \times 1$  Monkhorst-Pack k-point mesh. Rectangular supercells with 60 and 120 MoS<sub>2</sub> formula units are used in the calculation of the formation energy of Mo vacancies.

### 5.3 Kinetic Monte Carlo simulation

The KMC simulation follows the method described in the reference<sup>36</sup> with the parameters calculated via first-principles in our previous work<sup>30</sup>. The simulations start from a circular void, and are performed under chalcogen-rich conditions (see the Supporting Information for more details).

### 5.4 MOCVD growth of WSe<sub>2</sub>

Tungsten selenide is synthesized on (0001)-oriented sapphire substrates using tungsten hexacarbonyl and dimethylselenium precursors in a vertical cold wall reactor using an H<sub>2</sub> carrier gas. The samples were heated to 500°C and annealed for 15 min to drive off any water vapor. Subsequently, samples are heated to 800°C for synthesis of the WSe<sub>2</sub>. Upon reaching growth temperature the tungsten hexacarbonyl and dimethylselenium are introduced into the reaction chamber. Growth took place at 700 Torr and growth times were 30 min. The optimal Se/W precursor ratio for synthesis was approximately 20,000.

### 5.5 MBE growth and the characterization of Bi<sub>2</sub>Se<sub>3</sub>

The Bi<sub>2</sub>Se<sub>3</sub> thin films were grown by molecular beam epitaxy (MBE) in a V.G. Semicon V80H deposition chamber. C-plane sapphire substrates were purchased from University Wafer and ultrasonically cleaned in acetone, methanol, and isopropyl alcohol for 10 minutes each prior to loading into the MBE system. The sapphire samples were annealed at 600 °C for 90 min, and 750 °C for 10 min to degas and clean the surface before being cooled to the growth temperature. The Bi<sub>2</sub>Se<sub>3</sub> growth chamber is equipped with two Knudsen effusion cells for the evaporation of elemental Se and Bi, and *in situ* reflection high energy electron diffraction (RHEED) for characterization during growth. The sources were outgassed for 2 hours prior to the initiation of the Bi<sub>2</sub>Se<sub>3</sub> deposition. During the growth process, the chamber pressure was maintained at  $\sim 4 \times 10^{-10}$  mbar, and the resulting deposition rate was 1.2 nm/min. Raman spectra acquisition was performed using a Renishaw confocal Raman system. The laser excitation wavelength was 532 nm, with a laser power of 0.22 mW and a spot size of roughly 500 nm. X-ray diffraction peaks were identified by performing out-of-plane scans with a Rigaku Ultima-III X-Ray Diffractometer system. TEM cross-sectional samples were made by FIB-SEM Nova 200 with a lift-out method. A JEM-ARM200F transmission electron microscope operated at 200kV with probe aberration corrector was used for Bi<sub>2</sub>Se<sub>3</sub> cross-section imaging.

*Ex-situ* STM images were recorded using an Omicron variable temperature scanning probe microscopy (VT-SPM) integrated with a preparation chamber, and an X-ray/UV photoelectron spectrometer<sup>75</sup>. The base pressure in the STM chamber was kept in the  $\sim 10^{-10}$  mbar range. STM images were recorded at room temperature using an electrochemically etched W tips, and analyzed using WSxM software. The surface of Bi<sub>2</sub>Se<sub>3</sub> samples were protected with a Se cap, removed prior STM by in-situ annealing at 200 °C for 1 hour. X-ray photoelectron spectroscopy was accomplished using a monochromated Al K $\alpha$  source ( $h\nu = 1486.7$  eV) and an Omicron EA125 hemispherical analyzer described in detail elsewhere. The XPS spectra were fitted using the curve-fitting software AAnalyzer<sup>76</sup>.

## Conflicts of interest

The authors declare no competing financial interest.

## Statement of contributions

Y.N. conceived the idea, designed and performed the PFM simulations. W.V., L.C., P.-R.C., R.M.W., C.L.H. and K.C. planned and supervised the study. A.T.B. performed Bi<sub>2</sub>Se<sub>3</sub> synthesis and the characterizations of Bi<sub>2</sub>Se<sub>3</sub>. L.A.W. and R.Y. performed MBE growth and AFM characterizations of WSe<sub>2</sub>. S.M.E. and J.A.R. performed MOCVD synthesis of WSe<sub>2</sub>. R.A. and C.C. performed STM characterizations. Q.W. and M.K. performed STEM characterizations. Y.N., Y.Z. C.L. and C.Z. performed DFT calculations. Y.N., A.T.B. and Y.Z. wrote the manuscript. All the co-authors reviewed and revised the manuscript.

## Acknowledgements

This work was supported by the Center for Low Energy Systems Technology (LEAST), one of six centers supported by the STARnet

phase of the Focus Center Research Program (FCRP), a Semiconductor Research Corporation Program sponsored by MARCO and DARPA.

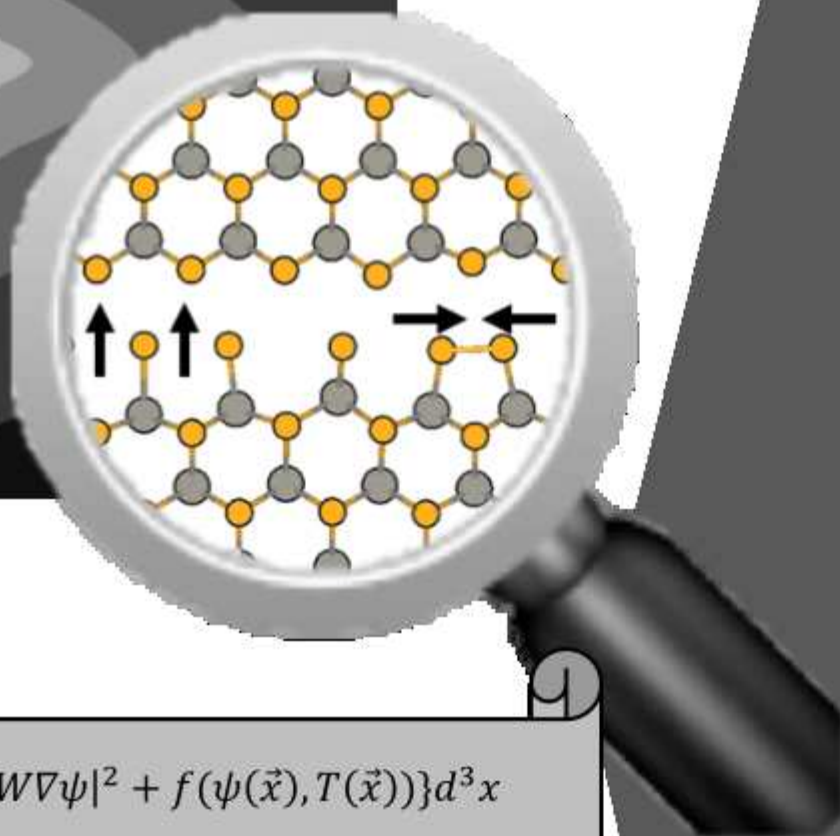
PRC appreciates the financial support by Leading Foreign Research Institute Recruitment Program through the National Research Foundation of Korea (NRF) funded by the Ministry of Science, ICT & Future Planning (MSIP) (2013K1A4A3055679).

The authors also thanks Texas Advaced Computing Center (TACC) for providing computation resources.

## Notes and references

- B. Radisavljevic, A. Radenovic, J. Brivio, V. Giacometti and A. Kis, *Nat. Nanotechnol.*, 2011, **6**, 147–150.
- Q. H. Wang, K. Kalantar-Zadeh, A. Kis, J. N. Coleman and M. S. Strano, *Nat. Nanotechnol.*, 2012, **7**, 699–712.
- S. Z. Butler, S. M. Hollen, L. Cao, Y. Cui, J. A. Gupta, H. R. Gutiérrez, T. F. Heinz, S. S. Hong, J. Huang, A. F. Ismach, E. Johnston-Halperin, M. Kuno, V. V. Plashnitsa, R. D. Robinson, R. S. Ruoff, S. Salahuddin, J. Shan, L. Shi, M. G. Spencer, M. Terrones, W. Windl and J. E. Goldberger, *ACS Nano*, 2013, **7**, 2898–2926.
- M. Chhowalla, H. S. Shin, G. Eda, L.-J. Li, K. P. Loh and H. Zhang, *Nat. Chem.*, 2013, **5**, 263–275.
- X. Qian, J. Liu, L. Fu and J. Li, *Science*, 2014, **346**, 1344–1347.
- D. Jariwala, V. K. Sangwan, L. J. Lauhon, T. J. Marks and M. C. Hersam, *ACS Nano*, 2014, **8**, 1102–1120.
- C. Zhang, S. KC, Y. Nie, C. Liang, W. G. Vandenberghe, R. C. Longo, Y. Zheng, F. Kong, S. Hong, R. M. Wallace *et al.*, *ACS Nano*, 2016, **10**, 7370–7375.
- C. Zhang, C. Gong, Y. Nie, K.-A. Min, C. Liang, Y. J. Oh, H. Zhang, W. Wang, S. Hong, L. Colombo *et al.*, *2D Mater.*, 2016, **4**, 015026.
- K. Novoselov, D. Jiang, F. Schedin, T. Booth, V. Khotkevich, S. Morozov and A. Geim, *Proc. Natl. Acad. Sci. USA*, 2005, **102**, 10451–10453.
- X. Li, W. Cai, J. An, S. Kim, J. Nah, D. Yang, R. Piner, A. Vellamakanni, I. Jung, E. Tutuc, S. K. Banerjee, L. Colombo and R. S. Ruoff, *Science*, 2009, **324**, 1312–1314.
- Y. Shi, W. Zhou, A.-Y. Lu, W. Fang, Y.-H. Lee, A. L. Hsu, S. M. Kim, K. K. Kim, H. Y. Yang, L.-J. Li, J.-C. Idrobo and J. Kong, *Nano Lett.*, 2012, **12**, 2784–2791.
- A. M. Van Der Zande, P. Y. Huang, D. A. Chenet, T. C. Berkelbach, Y. You, G.-H. Lee, T. F. Heinz, D. R. Reichman, D. A. Muller and J. C. Hone, *Nat. Mater.*, 2013, **12**, 554–561.
- S. Najmaei, Z. Liu, W. Zhou, X. Zou, G. Shi, S. Lei, B. I. Yakobson, J.-C. Idrobo, P. M. Ajayan and J. Lou, *Nat. Mater.*, 2013, **12**, 754–759.
- J.-K. Huang, J. Pu, C.-L. Hsu, M.-H. Chiu, Z.-Y. Juang, Y.-H. Chang, W.-H. Chang, Y. Iwasa, T. Takenobu and L.-J. Li, *ACS Nano*, 2013, **8**, 923–930.
- S. Wang, Y. Rong, Y. Fan, M. Pacios, H. Bhaskaran, K. He and J. H. Warner, *Chem. Mater.*, 2014, **26**, 6371–6379.
- K. Kang, S. Xie, L. Huang, Y. Han, P. Y. Huang, K. F. Mak, C.-J. Kim, D. Muller and J. Park, *Nature*, 2015, **520**, 656–660.
- S. M. Eichfeld, L. Hossain, Y.-C. Lin, A. F. Piasecki, B. Kupp, A. G. Birdwell, R. A. Burke, N. Lu, X. Peng, J. Li, A. Azcatl, S. McDonnell, R. M. Wallace, M. J. Kim, T. S. Mayer, J. M. Redwing and J. A. Robinson, *ACS Nano*, 2015, **9**, 2080–2087.
- S. Vishwanath, X. Liu, S. Rouvimov, P. C. Mende, A. Azcatl, S. McDonnell, R. M. Wallace, R. M. Feenstra, J. K. Furdyna, D. Jena and H. G. Xing, *2D Mater.*, 2015, **2**, 024007.
- R. Yue, A. T. Barton, H. Zhu, A. Azcatl, L. F. Pena, J. Wang, X. Peng, N. Lu, L. Cheng, R. Addou, S. McDonnell, L. Colombo, J. W. P. Hsu, J. Kim, M. J. Kim, R. M. Wallace and C. L. Hinkle, *ACS Nano*, 2015, **9**, 474–480.
- H. Li, Y. Li, A. Aljarb, Y. Shi and L.-J. Li, *Chem. Rev. ASAP*, 2017, **0**, null.
- J. Zhang, H. Yu, W. Chen, X. Tian, D. Liu, M. Cheng, G. Xie, W. Yang, R. Yang, X. Bai, D. Shi and G. Zhang, *ACS Nano*, 2014, **8**, 6024–6030.
- S. M. Eichfeld, V. O. Colon, Y. Nie, K. Cho and J. A. Robinson, *2D Mater.*, 2016, **3**, 025015.
- R. Yue, Y. Nie, L. A. Walsh, R. Addou, C. Liang, N. Lu, A. T. Barton, H. Zhu, Z. Che, D. Barrera *et al.*, *2D Mater.*, 2017, **4**, 045019.
- T. H. Ly, M.-H. Chiu, M.-Y. Li, J. Zhao, D. J. Perello, M. O. Cichocka, H. M. Oh, S. H. o. Chae, H. Y. Jeong, F. Yao, L.-J. Li and Y. H. Lee, *ACS Nano*, 2014, **8**, 11401–11408.
- O. Lehtinen, H.-P. Komsa, A. Pulkin, M. B. Whitwick, M.-W. Chen, T. Lehnert, M. J. Mohn, O. V. Yazyev, A. Kis, U. Kaiser and A. V. Krasheninnikov, *ACS Nano*, 2015, **9**, 3274–3283.
- J. Cheng, T. Jiang, Q. Ji, Y. Zhang, Z. Li, Y. Shan, Y. Zhang, X. Gong, W. Liu and S. Wu, *Adv. Mater.*, 2015, **27**, 4069–4074.
- V. I. Artyukhov, Z. Hu, Z. Zhang and B. I. Yakobson, *Nano Lett.*, 2016, **16**, 3696–3702.
- E. Meca, J. Lowengrub, H. Kim, C. Mattevi and V. B. Shenoy, *Nano Lett.*, 2013, **13**, 5692–5697.
- A. Govind Rajan, J. H. Warner, D. Blankschtein and M. S. Strano, *ACS Nano*, 2016, **10**, 4330–4344.
- Y. Nie, C. Liang, K. Zhang, R. Zhao, S. M. Eichfeld, P.-R. Cha, L. Colombo, J. A. Robinson, R. M. Wallace and K. Cho, *2D Mater.*, 2016, **3**, 025029.
- W. Zhou, X. Zou, S. Najmaei, Z. Liu, Y. Shi, J. Kong, J. Lou, P. M. Ajayan, B. I. Yakobson and J.-C. Idrobo, *Nano Lett.*, 2013, **13**, 2615–2622.
- H.-P. Komsa, S. Kurasch, O. Lehtinen, U. Kaiser and A. V. Krasheninnikov, *Phys. Rev. B*, 2013, **88**, 035301.
- S. McDonnell, R. Addou, C. Buie, R. M. Wallace and C. L. Hinkle, *ACS Nano*, 2014, **8**, 2880–2888.
- M. J. Cuddy, K. P. Arkill, Z. W. Wang, H.-P. Komsa, A. V. Krasheninnikov and R. E. Palmer, *Nanoscale*, 2014, **6**, 12463–12469.
- S.-L. Shang, G. Lindwall, Y. Wang, J. M. Redwing, T. Anderson and Z.-K. Liu, *Nano Lett.*, 2016, **16**, 5742–5750.
- Y. Nie, C. Liang, P.-R. Cha, L. Colombo, R. M. Wallace and K. Cho, *Sci. Rep.*, 2017, **7**, 1–13.
- A. Koma, K. Ueno and K. Saiki, *J. Cryst. Growth*, 1991, **111**, 1029–1032.

- 38 M. I. B. Utama, Q. Zhang, J. Zhang, Y. Yuan, F. J. Belarre, J. Arbiol and Q. Xiong, *Nanoscale*, 2013, **5**, 3570–3588.
- 39 Y. Liu, R. Ghosh, D. Wu, A. Ismach, R. Ruoff and K. Lai, *Nano Lett.*, 2014, **14**, 4682–4686.
- 40 Y. Cheng, K. Yao, Y. Yang, L. Li, Y. Yao, Q. Wang, X. Zhang, Y. Han and U. Schwingenschlöggl, *RSC Adv.*, 2013, **3**, 17287–17293.
- 41 Y. Yu, S.-Y. Huang, Y. Li, S. N. Steinmann, W. Yang and L. Cao, *Nano Lett.*, 2014, **14**, 553–558.
- 42 C. Yuan, Y. Cao, X. Luo, T. Yu, Z. Huang, B. Xu, Y. Yang, Q. Li, G. Gu and W. Lei, *Nanoscale*, 2015, **7**, 17468–17472.
- 43 A. Roy, R. Ghosh, A. Rai, A. Sanne, K. Kim, H. C. P. Movva, R. Dey, T. Pramanik, S. C. owdhury, E. Tutuc and S. K. Banerjee, *Appl. Phys. Lett.*, 2017, **110**, 201905.
- 44 Y. Ji, B. Calderon, Y. Han, P. Cueva, N. R. Jungwirth, h. a. alsalman, J. Hwang, G. D. Fuchs, D. A. Muller and M. G. Spencer, *ACS Nano*, 2017, 12057 – 12066.
- 45 M. J. Shearer, L. Samad, Y. Zhang, Y. Zhao, A. Puzos, K. W. Eliceiri, J. C. Wright, R. o. J. Hamers and S. Jin, *J. Am. Chem. Soc.*, 2017, **139**, 3496–3504.
- 46 S. A. Morin, A. Forticaux, M. J. Bierman and S. Jin, *Nano Lett.*, 2011, **11**, 4449–4455.
- 47 F. Meng, S. A. Morin, A. Forticaux and S. Jin, *Acc. Chem. Res.*, 2013, **46**, 1616–1626.
- 48 R. Suzuki, M. Sakano, Y. Zhang, R. Akashi, D. Morikawa, A. Harasawa, K. Yaji, K. Kuroda, K. Miyamoto, T. Okuda *et al.*, *Nat. Nanotechnol.*, 2014, **9**, 611–617.
- 49 L. Zhang, K. Liu, A. B. Wong, J. Kim, X. Hong, C. Liu, T. Cao, S. G. Louie, F. Wang and P. Yang, *Nano Lett.*, 2014, **14**, 6418–6423.
- 50 L. Chen, B. Liu, A. N. Abbas, Y. Ma, X. Fang, Y. Liu and C. Zhou, *ACS Nano*, 2014, **8**, 11543–11551.
- 51 A. Zhuang, J.-J. Li, Y.-C. Wang, X. Wen, Y. Lin, B. Xiang, X. Wang and J. Zeng, *Angew. Chem. Int. Ed.*, 2014, **53**, 6425–6429.
- 52 A. Forticaux, L. Dang, H. Liang and S. Jin, *Nano Lett.*, 2015, **15**, 3403–3409.
- 53 P. V. Sarma, P. D. Patil, P. K. Barman, R. N. Kini and M. M. Shaijumon, *RSC Adv.*, 2016, **6**, 376–382.
- 54 T. H. Ly, J. Zhao, H. Kim, G. H. Han, H. Nam and Y. H. Lee, *Adv. Mater.*, 2016, **28**, 7723–7728.
- 55 J. Wu, Z. Hu, Z. Jin, S. Lei, H. Guo, K. Chatterjee, J. Zhang, Y. Yang, B. Li, Y. Liu *et al.*, *Adv. Mater. Interfaces*, 2016, **3**, 1 – 8.
- 56 X. Fan, Y. Jiang, X. Zhuang, H. Liu, T. Xu, W. Zheng, P. Fan, H. Li, X. Wu, X. Z hu, Q. Zhang, H. Zhou, W. Hu, X. Wang, L. Sun, X. Duan and A. Pan, *ACS Nano*, 2017, **11**, 4892–4898.
- 57 A. G. Shtukenberg, Z. Zhu, Z. An, M. Bhandari, P. Song, B. Kahr and M. D. Ward, *Proc. of the Natl. Acad. Sci. USA*, 2013, **110**, 17195–17198.
- 58 P. C. Hohenberg and B. I. Halperin, *Rev. Mod. Phys.*, 1977, **49**, 435–479.
- 59 A. Karma and M. Plapp, *Phys. Rev. Lett.*, 1998, **81**, 4444.
- 60 A. Karma and W.-J. Rappel, *Phys. Rev. E*, 1998, **57**, 4323–4349.
- 61 M. Fleck, L. Mushongera, D. Pilipenko, K. Ankit and H. Emmerich, *Eur. Phys. J. Plus*, 2011, **126**, 1–11.
- 62 G. B. McFadden, A. A. Wheeler, R. J. Braun, S. R. Coriell and R. F. Sekerka, *Phys. Rev. E*, 1993, **48**, 2016–2024.
- 63 G. Caginalp, *Phys. Rev. A*, 1989, **39**, 5887.
- 64 W.-K. Burton, N. Cabrera and F. Frank, *Philos. Trans. R. Soc. London, Ser. A*, 1951, **243**, 299–358.
- 65 F. C. Frank and W. T. Read Jr, *Phys. Rev.*, 1950, **79**, 722.
- 66 F. Nabarro, *Philos. Mag. A*, 1986, **54**, 577–582.
- 67 T. P. Ginley and S. Law, *J. Vac. Sci. Technol. B*, 2016, **34**, 02L105.
- 68 X. Zhong, A. G. Shtukenberg, T. Hueckel, B. Kahr and M. D. Ward, *Cryst. Growth Des.*, 2018, **18**, 318–323.
- 69 T. H. Ly, S. J. Yun, Q. H. Thi and J. Zhao, *ACS Nano*, 2017, **11**, 7534–7541.
- 70 H. Ye, J. Zhou, D. Er, C. Price, Z. Yu, Y. Liu, J. S. Lowengrub, J. Lou, Z. Liu and V. B. Shenoy, *ACS Nano*, 2017, 12780 – 12788.
- 71 T. A. Davis and Y. Hu, *ACM Trans. Math. Softw.*, 2011, **38**, 1.
- 72 G. Kresse and J. Furthmüller, *Phys. Rev. B*, 1996, **54**, 11169–11186.
- 73 G. Kresse and D. Joubert, *Phys. Rev. B*, 1999, **59**, 1758–1775.
- 74 J. P. Perdew, K. Burke and M. Ernzerhof, *Phys. Rev. Lett.*, 1996, **77**, 3865–3868.
- 75 R. M. Wallace, *ECS Trans.*, 2014, **64**, 109–116.
- 76 A. Herrera-Gomez, A. Hegedus and P. Meissner, *Appl. Phys. Lett.*, 2002, **81**, 1014–1016.



$$H[\psi, T] = \int_V \left\{ \frac{1}{2} |W \nabla \psi|^2 + f(\psi(\vec{x}), T(\vec{x})) \right\} d^3x$$

$$\tau_\psi \frac{\partial \psi}{\partial t} = - \frac{\delta H}{\delta \psi}$$

$$\frac{\partial u}{\partial t} = D \nabla^2 u - \frac{u}{\tau_s} + F - \frac{1}{2} \frac{\partial \psi}{\partial t}$$

